Si doping in MOCVD grown (010) β-(Al_xGa_{1-x})₂O₃ thin films

A F M Anhar Uddin Bhuiyan^{1,a)}, Zixuan Feng¹, Lingyu Meng¹, Andreas Fiedler¹, Hsien-Lien Huang², Adam T. Neal³, Erich Steinbrunner³, Shin Mou³, Jinwoo Hwang², Siddharth Rajan^{1,2} and Hongping Zhao^{1,2,b)}

¹Department of Electrical and Computer Engineering, The Ohio State University, Columbus, OH 43210, USA
²Department of Materials Science and Engineering, The Ohio State University, Columbus, OH 43210, USA
³Air Force Research Laboratory, Materials and Manufacturing Directorate, Wright-Patterson Air Force Base,
OH 45433, USA

^{a)}Email: <u>bhuiyan.13@osu.edu</u> ^{b)}Corresponding author Email: <u>zhao.2592@osu.edu</u>

Abstract

In this work, the structural and electrical properties of metalorganic chemical vapor deposited Si doped β-(Al_xGa_{1-x})₂O₃ thin films grown on (010) β-Ga₂O₃ substrates are investigated as a function of Al composition. The room temperature Hall mobility of 101 cm²/V·s and low temperature peak mobility (T=65K) of 1157 cm²/V·s at carrier concentrations of 6.56×10¹⁷ cm⁻³ and 2.30×10¹⁷ cm⁻³ ³ are measured from 6% Al composition samples, respectively. The quantitative secondary ion mass spectroscopy (SIMS) characterization reveals a strong dependence of Si and other unintentional impurity such as C, H and Cl concentrations in β-(Al_xGa_{1-x})₂O₃ thin films with different Al compositions. Higher Al compositions in β-(Al_xGa_{1-x})₂O₃ result in lower net carrier concentrations due to the reduction of Si incorporation efficiency and the increase of C and H impurity levels that act as compensating acceptors in β-(Al_xGa_{1-x})₂O₃ films. Lowering the growth chamber pressure reduces Si concentrations in β-(Al_xGa_{1-x})₂O₃ films due to the increase of Al compositions as evidenced by comprehensive SIMS and Hall characterizations. Due to the increase of lattice mismatch between the epi-film and substrate, higher Al compositions lead to cracking in β-(Al_xGa_{1-x})₂O₃ films grown on β-Ga₂O₃ substrates. The (100) cleavage plane is identified as a major cracking plane limiting the growth of high-quality Si doped (010) β-(Al_xGa_{1-x})₂O₃ films

beyond the critical thicknesses, which leads to highly anisotropic and inhomogeneous behaviors in terms of conductivity.

Keywords: Ultrawide bandgap semiconductor, β-(Al_xGa_{1-x})₂O₃ thin films, Si doping, metalorganic chemical vapor deposition, cracking

I. Introduction

β-Ga₂O₃ has been considered as a promising semiconductor material for next-generation high power electronic devices due to its ultra-wide bandgap energy (4.8-4.9 eV), theoretically predicted high breakdown field strength (8 MV/cm), and for the ease of mass production of free-standing single crystal native substrates [1,2]. The demonstration of n-type doping in β-Ga₂O₃ over a wide range of electron concentrations ($10^{16} - 10^{20}$ cm⁻³) with decent transport properties such as the mobility close to 200 cm²/V.s at room temperature and >10⁴ cm²/V·s at cryo-temperature with ultra-low background concentration (10^{14}) reveal this material's immense potential in high power electronic and deep ultraviolet optoelectronic applications [3-19]. Another key advantage of β-Ga₂O₃ is its capability of the bandgap engineering by alloying with Al₂O₃ which can extend the bandgap energy up to 7.24 eV in monoclinic phase [20]. Due to the tunability of bandgap energy over a wide range, β-(Al₃Ga_{1-x})₂O₃ alloys possess a great promise for next generation high power and radio frequency electronic applications.

Considering the enormous potential of β -(Al_xGa_{1-x})₂O₃ alloys in electronic and optoelectronic applications, several studies have been conducted on the development of β -(Al_xGa_{1-x})₂O₃ epitaxy [21-34] and β -(Al_xGa_{1-x})₂O₃/ β -Ga₂O₃ heterostructure-based lateral devices [35-39] grown by different growth techniques including molecular beam epitaxy (MBE) [21-23] and metalorganic chemical vapor deposition (MOCVD) [24-34]. MOCVD grown phase pure β -(Al_xGa_{1-x})₂O₃ thin

films on (010) (x ≤ 35%) [24,25,29,33], (100) (x ≤ 52%) [26,27] and ($\overline{2}$ 01) (x ≤ 48%) [28,33] oriented β-Ga₂O₃ substrates have been demonstrated with a great control of elemental compositions, uniformity, and high purity. β-(Al_xGa_{1-x})₂O₃ alloy with < 80% Al composition is predicted to have a breakdown field strength up to 16 MV/cm [40], which is significantly higher than the fields achievable from SiC or GaN based devices, even with nominally lower content of Al. Moreover, high-Al composition in phase pure β-(Al_xGa_{1-x})₂O₃ layer is advantageous as it offers opportunity to generate two-dimensional electron gas (2DEG) by modulation doping at the β-(Al_xGa_{1-x})₂O₃/β-Ga₂O₃ interface owing to its tunable and large conduction band offset [35-39]. Excellent transport properties have already been demonstrated for modulation doped field effect transistors (MODFETs) based on β-(Al_xGa_{1-x})₂O₃/β-Ga₂O₃ heterostructures. A room temperature mobility of < 180 cm²/Vs and a cryo-temperature peak mobility of < 2790 cm²/Vs were measured at a 2DEG sheet charge density of < 5 × 10¹² cm⁻² for Al compositions x ≤ 0.20 [35,36]. The successful operation of these MODFET devices shows great potential for developing high performance transistors using β-(Al_xGa_{1-x})₂O₃/β-Ga₂O₃ (x ≤ 0.20) heterostructures.

While several studies on the epitaxial growth of β -(Al_xGa_{1-x})₂O₃ thin films over a wide range of Al compositions have been reported, the investigation of the n-type doping of β -(Al_xGa_{1-x})₂O₃ is still limited. Recently, theoretical studies based on hybrid density functional theory calculations have predicted Si as the most efficient shallow donor for high Al-content β -(Al_xGa_{1-x})₂O₃ alloys, effective up to 70-85% Al compositions [41,42]. Our previous experimental study on MOCVD grown Si doped β -(Al_xGa_{1-x})₂O₃ thin films grown with 6.3-33.4% Al compositions exhibited promising room temperature (RT) mobility (42-108 cm²/Vs) at doping concentrations ranging between 10^{17} - 10^{18} cm⁻³ [24]. Another investigation on the uniformly Si doped MOCVD β -(Al_{0.26}Ga_{0.74})₂O₃ films showed higher carrier concentrations of 6×10^{18} - 7.3×10^{19} cm⁻³ with

corresponding RT mobilities of 53-27 cm²/V.s [43]. Although these studies indicated the possibility for n-type Si doping in β -(Al_xGa_{1-x})₂O₃ thin films for a wide range of doping concentrations and Al compositions, the measured transport results can be significantly impacted by the formation of a modulation doped channel in β -Ga₂O₃ and by the electron accumulation at β -(Al_xGa_{1-x})₂O₃/ β -Ga₂O₃ interfaces. The direct growth of Si doped β -(Al_xGa_{1-x})₂O₃ layer on undoped β -Ga₂O₃ or β -(Al_xGa_{1-x})₂O₃ buffer layer can induce complications for characterizing the electrical properties of β -(Al_xGa_{1-x})₂O₃ and can also affect the device performances by causing higher buffer leakage current in lateral devices. Instead, growing a uniformly Si doped β -(Al_xGa_{1-x})₂O₃ layer on top of a semi-insulating buffer layer may compensate the charge accumulation at the interface, allowing for precise electrical measurement in the doped β -(Al_xGa_{1-x})₂O₃ layer.

The Mg-doped semi-insulating β -Ga₂O₃ buffer layer was found to effectively compensate the charge accumulation at the substrate-epilayer interface from our recent study on MOCVD grown β -Ga₂O₃ films [17]. In this work, Si doped β -(Al_xGa_{1-x})₂O₃ films are grown on top of in-situ grown Mg-doped β -Ga₂O₃ buffer layer to suppress the interface charge. While our previous study on MOCVD epitaxy of β -(Al_xGa_{1-x})₂O₃ reported the preliminary transport data such as the mobility and carrier concentration of β -(Al_xGa_{1-x})₂O₃ with different Al compositions [24], the influence of Si-doping concentration on structural and electrical properties of β -(Al_xGa_{1-x})₂O₃ thin films as a function of Al composition is not systematically studied. The current work investigates the fundamental properties of Si doping in MOCVD grown β -(Al_xGa_{1-x})₂O₃ thin films for different Al compositions (x = 6%, 11% and 18%) in terms of physical, structural, morphological, and electrical properties. The fundamental challenges associated with the formation of cracking and increased impurity concentrations in β -(Al_xGa_{1-x})₂O₃ thin films due to higher Al incorporation are also systematically investigated as a function of Al composition. The characteristics of Si doping

in β-(Al_xGa_{1-x})₂O₃ with high Al compositions are investigated using comprehensive characterization via x-ray diffraction (XRD), secondary ion mass spectroscopy (SIMS), high resolution scanning transmission electron microscopy (STEM), optical and atomic force microscopy (AFM) and Hall transport measurements.

II. Experimental details

II.A MOCVD growth of Si doped β-(Al_xGa_{1-x})₂O₃ thin films

The β -(Al_xGa_{1-x})₂O₃ films with 6%, 11% and 18% Al compositions were grown on Fe doped semi-insulating (010) β-Ga₂O₃ substrates by using Agnitron Technology Agilis R&D MOCVD system. The β-Ga₂O₃ substrates were purchased from Novel Crystal Technology, Inc. The Si doped ~350-450 nm thick β-(Al_xGa_{1-x})₂O₃ films were grown on ~65 nm thick Mg-doped semiinsulating β-Ga₂O₃ buffer layer on top of (010) β-Ga₂O₃ substrates. The Mg doped β-Ga₂O₃ buffer layer was grown at a growth temperature of 700 °C with a chamber pressure of 60 torr. The growth temperature of 880 °C and the chamber pressure of 20 torr were used to grow the β-(Al_xGa_{1-x})₂O₃ layers on top of Mg doped β-Ga₂O₃ buffer layer. Triethylgallium (TEGa), Trimethylaluminum (TMAl), Bis-(cyclopentadienyl)-magnesium (Cp₂Mg) and pure O₂ were used as Ga, Al, Mg and O precursors, respectively. Ar was used as the carrier gas. The Mg/Ga molar flow rate ratio was 6.69 x 10⁻³. Al composition of 6%-18% was obtained by varying the [TMA1]/[TEGa+TMA1] molar flow rate ratio from 1.08% to 3.71%. The O₂ flow rate was set at 500 sccm for all growths. Silicon dopants were introduced into the chamber by flowing diluted silane (SiH₄). Different doping concentrations of β-(Al_xGa_{1-x})₂O₃ thin films were obtained by controlling the mass flow controllers in the silane and dilution lines. The silane flow rate was tuned from 0.53 to 100.1 nmol/min. All the substrates were ex-situ cleaned by solvent before loading to the MOCVD reactor. Any potential contamination on the substrate surface was removed by performing a high temperature in-situ annealing at 920 °C for 5 mins duration under O₂ atmosphere prior the growth.

II.B Material Characterization

The Al composition and crystalline structure of the β -(Al_xGa_{1-x})₂O₃ films were evaluated by high resolution XRD by using a Bruker D8 Discover (Cu Kα source, λ=1.5418 Å). Surface morphologies and roughness were characterized by optical (Huvitz HRM-300) and atomic force (AFM, Bruker Icon 3) microscopy. The β-(Al_xGa_{1-x})₂O₃ film thicknesses were estimated from the cross-sectional field emission scanning electron microscope (FESEM) images of the reference (Al_xGa_{1-x})₂O₃ samples grown on the co-loaded c-plane sapphire substrates and by using high resolution STEM imaging. A Thermo Fisher Scientific Themis-Z scanning transmission electron microscope (operated at 200 kV) was used for high resolution STEM imaging. The elemental concentrations of β-(Al_xGa_{1-x})₂O₃ were characterized by SIMS. An HMS 3000 Fast Hall measurement system (Ecopia) was used to measure the carrier concentration and electron Hall mobility at room temperature. 20/100 nm Ti/Au contacts were deposited on four corners of the sample to create the van der Pauw setup for Hall measurement. Temperature dependent Hall measurement was performed using two custom built systems. For the measurement below room temperature, an electromagnet with a vacuum cryostat with closed cycle helium (He) refrigerator was used. An electromagnet with a quartz tube and silicon carbide heater was used for the measurement above room temperature.

III. Results and Discussions

Figure 1(a) shows the schematic of the Si doped β -(Al_xGa_{1-x})₂O₃ films grown with [TMAl]/[TEGa+TMAl] molar flow rate ratio of 1.08%, 2.21% and 3.71% on 65 nm thick Mg

doped β-Ga₂O₃ buffer layer. XRD ω -2θ scans for the films grown with different molar flow ratios are shown in Figure 1(b). The Al compositions of β-(Al_xGa_{1-x})₂O₃ films increase monotonically from 6% to 18% as the [TMAl]/[TEGa+TMAl] molar flow rate ratio increases from 1.08% to 3.71%. The rocking curve full width at half maximum (FWHMs) are measured as 50-105 arc sec for different samples. The sharp and high intensity diffraction peaks from (020) reflection of β-(Al_xGa_{1-x})₂O₃ films with narrow rocking curve FWHMs indicate the growth of high-quality Si doped β-(Al_xGa_{1-x})₂O₃ films on β-Ga₂O₃ substrates.

To investigate the influence of different Al compositions on Si, C, H and Cl impurity concentrations, quantitative SIMS characterization was carried out on a multi-layer stack consisting of Si doped β -(Al_xGa_{1-x})₂O₃ (x = 6% and 18%) and UID β -Ga₂O₃ layers as shown in the schematic in Figure 2(a). Each Si doped β-(Al_xGa_{1-x})₂O₃ layers were grown with [TMA1]/[TEGa+TMA1] molar flow rate ratio of 1.08% and 3.71% which correspond to the Al composition of 6% and 18%, respectively. The silane flow rate in both β-(Al_xGa_{1-x})₂O₃ sub layers was fixed at 0.53 nmole/min. Between the two β -(Al_xGa_{1-x})₂O₃ sub layers, an unintentionally doped ~200 nm thick β-Ga₂O₃ layer was inserted to analyze the Si diffusion profile. SIMS depth profile reveals a symmetrical distribution of Si concentration on both sides as shown in Figure 2(b), indicating that the broadening of the Si is likely from diffusion. Si is considered as the most promising donor dopant in β -(Al_xGa_{1-x})₂O₃ thin films [41,42]. Si doping level as a function of Al composition is also studied by quantitative SIMS characterization. The Si concentration decreases from 8×10^{17} to 5×10^{17} cm⁻³ as the Al composition increases from 6% to 18%. While hybrid density functional theory (DFT) revealed that the Si acts as a shallow donor in β-(Al_xGa_{1-x})₂O₃ up to high Al concentrations (x < 70-85%) [41,42], the Si depth profile shows that the Si incorporation efficiency reduces as the Al composition in β -(Al_xGa_{1-x})₂O₃ increases. The secondary ion intensity

of Al shows a noticeable increase as [TMAl]/[TEGa+TMAl] molar flow ratio increases from 1.08% to 3.71%, indicating higher Al incorporation for higher molar flow ratio. Table 1 lists the Si, H, C and Cl levels in β -(Al_xGa_{1-x})₂O₃ layers with 6% and 18% Al compositions extracted from SIMS depth profiles. While Si incorporation efficiency in the alloy reduces due to higher Al incorporation, the concentrations of C, H and Cl impurities which are incorporated unintentionally are found to increase monotonically with the increase of Al compositions.

The influence on the incorporations of Si, C and H impurities for different Al compositions are also investigated by Hall measurements. Table 2 lists the room temperature Hall mobility and carrier concentrations measured from β-(Al_xGa_{1-x})₂O₃ films with Al compositions of 6% and 18% each for two different silane flow rates (5.84 and 14.35 nmole/min). With the increase of silane flow rate, the carrier concentration is found to increase for both samples with different Al composition. For silane flow rate of 5.84 nmole/min, the carrier concentration decreases from 4.90×10^{18} to 2.46×10^{15} cm⁻³ as the Al composition increases from 6% to 18%. A similar trend is also observed in case of 14.35 nmole/min silane flow rate. The carrier concentration reduces from 1.54×10¹⁹ to 2.11×10¹⁷ cm⁻³ with the increase of Al composition from 6% to 18%. The reduction of the measured Hall carrier concentration is consistent with the SIMS result (Figure 2(b)), which reveals that the Si incorporation efficiency reduces for higher Al concentration. Additionally, the increase of carbon and hydrogen impurity concentrations which act as compensating acceptors in β -(Al_xGa_{1-x})₂O₃ [42] also contribute to the reduction of net carrier concentrations measured by Hall measurements. The role of carbon and hydrogen impurities in limiting the n-type doping of β-(Al_xGa_{1-x})₂O₃ has been discussed recently by DFT calculations, indicating that the Si can be compensated by hydrogen at 1% Al or by carbon on cation sites at 5% Al compositions [42]. Substitutional carbon on a cation/oxygen site acts as a shallow donor in Ga₂O₃ as its positive charge

states are stable over the entire Ga₂O₃ bandgap which was predicted by theoretical study [44]. However, experimentally in our MOCVD grown high quality β-Ga₂O₃ homoepitaxial films [6], the Si concentration extracted from quantitative SIMS characterization matched well with the net N_d-N_a concentration, regardless of the existence of C background level, implying that C may not act as an active shallow donor in β-Ga₂O₃. While the growth conditions may also influence the role of C incorporated in β-Ga₂O₃, further investigation is required to confirm about the exact state of C in β-Ga₂O₃ [45,46]. Nevertheless, both C and H turn into compensating acceptors in β-(Al_xGa_{1-x})₂O₃ as the band gap widens due to higher Al incorporation, predicted by recent DFT calculations [42]. As compared to configurations such as the carbon occupying the octahedral cation sites or the oxygen sites, the C on the tetrahedral Ga site is found to be most stable in the positive charge state within Ga₂O₃ bandgap from DFT studies, deriving that C act as a shallow donor in Ga₂O₃. Similar to Ga₂O₃, the theoretical DFT calculations also predicted that carbon impurity prefers to occupy the substitutional tetrahedral cation site in monoclinic θ -Al₂O₃. In case of neutral charge state of $C_{Al(I)}$ (C on tetrahedral site) in θ -Al₂O₃, carbon moves beyond the plane of its oxygen neighbors towards a next-nearest Al(1) neighbor, causing a reduction of the C-Al distance from 3.5 to 2.6 Å. As a result, the charge of the localized state is confined between the carbon and that next-nearest-neighbor Al atom, indicating that C_{Al(I)} (with a corresponding Kohn-Sham state lying 4.42 eV below the conduction band minimum) is not a shallow donor in θ -Al₂O₃. By interpolating the (+/-) charge-state transition level of the C_(I) negative-U center (carbon substituting the tetrahedral Ga or Al site) between β -Ga₂O₃ and θ -Al₂O₃, carbon is found to act as acceptor with only 5% Al incorporation. On the other hand, carbon replacing the octahedral Ga or Al site $(C_{(II)})$ starts acting as an acceptor at > 51% Al compositions. However, carbon on oxygen sites (Co) are predicted to act as compensating acceptor for both Ga₂O₃ and Al₂O₃ under n-type doping conditions. Another common impurity in MOCVD growth system- hydrogen also acts as compensating acceptor in θ -Al₂O₃ as they are found to be stabilized in negative charge states, while all configurations of H substituting on the O site or interstitial site are found to act as shallow donor in β-Ga₂O₃. In addition, recent DFT calculation also predicted that the Al energetically prefers to occupy the octahedral Ga₂ site and is forced to occupy the tetrahedral Ga₁ site when the Al composition in β-(Al_xGa_{1-x})₂O₃ increases [30]. However, due to the surface reconstructions and kinetic limitations during the epitaxial growth, Al atoms are observed to occupy both octahedral and tetrahedral sites in β -(Al_xGa_{1-x})₂O₃ alloy, eventually leading to a structure with higher energy by the increase of total number of Al atoms substituting on the Ga₁ site. The lack of control over Al site incorporation results in the formation of extended (planar) defects. The divacancyinterstitial complexes, comprising of one cation interstitial atom paired with two cation vacancies, were predicted to be compensating acceptors in β-Ga₂O₃ [47]. The higher density of such planar defects in β-(Al_xGa_{1-x})₂O₃ alloy driven by the local increase of Al atoms might also contribute as compensators in Si doped β-(Al_xGa_{1-x})₂O₃ thin films. Experimentally, the lower Si incorporation efficiency along with higher level of compensations due to the increase of C and H impurity concentrations and planer defects can potentially contribute to the reduction of effective net doping in β -(Al_xGa_{1-x})₂O₃ films as evidenced by the comprehensive characterization of room temperature Hall measurements and SIMS. Along with the reduction of carrier concentration, the room temperature Hall mobility also drastically decreases with the increase of Al composition for both cases with different silane flows, which can be attributed to the increase of both alloy scattering and divacancy - cation interstitial defect density developed due to incorporation of higher Al concentration [24].

As the Si doping in β -(Al_xGa_{1-x})₂O₃ films with higher Al compositions are found to be challenging due to the increase of impurity concentrations, the role of different silane flow rates on transport properties of β-(Al_xGa_{1-x})₂O₃ films with relatively low Al compositions are investigated. Figure 3(a) shows the room-temperature Hall mobility and resistivity versus carrier concentration for β-(Al_xGa_{1-x})₂O₃ films grown with 6% Al composition for different silane flow rates ranging between 1.17-14.35 nmole/min. Increasing the silane flow from 1.17 to 14.35 nmole/min leads to the increase of carrier concentration from 6.56×10¹⁷ to 1.54×10¹⁹ cm⁻³. However, the Hall resistivity and the room temperature mobilities are found to decrease with increasing silane flow. As the doping concentration increases from 6.56×10^{17} to 1.54×10^{19} cm⁻³, the increased ionized impurity scattering becomes the dominant factor [3], which limits the roomtemperature mobility from 101 to 54 cm²/V.s. Following the room temperature Hall measurements, a selected representative 6% Al composition sample was characterized by temperature-dependent Hall measurement in the van-der-Pauw geometry to probe the donor activation energy, as shown in Figure 3(b) and 3(c). The temperature was varied from 40 to 300 K. The room-temperature Hall carrier mobility was measured as 101 cm²/V·s at a carrier concentration of 6.56×10¹⁷ cm⁻³. A peak mobility of 1157 cm²/V·s at a carrier concentration of 2.30×10¹⁷ cm⁻³ was measured at 65K. The donor activation energy (E_D) of 8 meV with donor (N_D) and compensation (N_A) concentrations of 1.15×10^{18} cm⁻³ and $\sim 4 \times 10^{16}$ cm⁻³, respectively, were extracted by fitting the temperature dependent transport data using the charge neutrality equation $(n + N_A = \frac{N_D}{1 + 2e^{-(E_D - E_F)}/k_B T})$, where N_A is the concentration of acceptors acting as compensators, N_D is the donor concentration, and E_D is the donor activation energy. The extracted activation energy of 8 meV for 6% Al composition sample is found to be close to the Si donor energy of β-Ga₂O₃ with similar doping density [48]. It is worth noting that the increase of Al composition can result in higher Si donor activation energy

in β-(Al_xGa_{1-x})₂O₃ due to the widening of the bandgap, which is clearly evidenced by the increase of donor activation energy from 8 to 36 meV, extracted from 6% and 18% Al composition samples, respectively, as shown later in Figure 4. Apart from the donor activation energy, the compensation concentrations extracted from the fitted data are also observed to increase from \sim 4×10¹⁶ to \sim 8×10¹⁶ cm⁻³ as the Al composition in β-(Al_xGa_{1-x})₂O₃ films increases from 6% to 18% (Figure 4), which is consistent with the results from SIMS characterization. Previously, the Si donor energy of β-Ga₂O₃ was found to decease with the increase of carrier density [48]. The Si donor activation energy of 16 meV from a β-(Al_{0.06}Ga_{0.94})₂O₃ film grown with a doping concentration of 1.98×10¹⁷ cm⁻³ was also extracted from the temperature dependent Hall measurement. As the doping concentration of β -(Al_{0.06}Ga_{0.94})₂O₃ decreases from 6.56×10^{17} cm⁻³ to 1.98×10^{17} cm⁻³, the donor activation energy was found to increase from 8 to 16 meV, which is consistent with the findings from β-Ga₂O₃ films investigated with different carrier concentrations [48]. Similar trend of a sharp reduction of Si activation energy with the increase in Si doping concentration was also observed in highly Si-doped (5.2x10 $^{18}\ cm^{-3} < N_d < 1.5x10^{19}\ cm^{-3})$ AlGaN films grown with 70% Al composition [49].

The growth of Si doped β -(Al_xGa_{1-x})₂O₃ films on unintentionally doped β -Ga₂O₃ buffer layer can lead to the formation of a modulation doped channel in β -Ga₂O₃ or electron accumulation at β -(Al_xGa_{1-x})₂O₃/ β -Ga₂O₃ interfaces. In addition, the significant peak of Si accumulation at the epilayer/substrate interface, as observed in Figure 2(b), can also add complications in transport characteristics. Such strong Si peak at the substrate growth interface was also observed in previous studies on homoepitaxial β -Ga₂O₃ thin films [3,6,17]. Owing to its lowest formation energy as compared to other cation site acceptors, Mg is considered as one of the most promising acceptors in β -Ga₂O₃ with relatively shallow acceptor level [50]. Mg doped β -Ga₂O₃ buffer layer was found

to be highly effective in suppressing the accumulated charges from epi-layer/substrate interface [17]. In this work, the Si doped β -(Al_xGa_{1-x})₂O₃ films were grown on Mg-doped β -Ga₂O₃ buffer layer to compensate the charges from the epi-layer/substrate and β-(Al_xGa_{1-x})₂O₃/β-Ga₂O₃ interfaces. The role of Mg-doped β-Ga₂O₃ buffer layer in suppressing the interface charges as compared to the UID β-Ga₂O₃ layer are probed by the temperature dependent carrier concentration. Figure 4 shows the carrier concentration vs. temperature profile for Si doped β-(Al_xGa_{1-x})₂O₃ films grown on top of Mg-doped β -Ga₂O₃ buffer layer and UID β -Ga₂O₃ buffer layer with x = 6% and 18%, respectively. The Hall carrier concentrations of 6.56×10¹⁷ cm⁻³ and 6.50×10¹⁷ cm⁻³ were measured at room temperature for the samples, respectively. The β-(Al_{0.18}Ga_{0.82})₂O₃ film grown on top of UID β-Ga₂O₃ buffer layer indicates a significant amount of interface charges as evidenced by the appearance of higher carrier density profile at low temperature region (higher divergence between the model and experimental data) in Figure 4 as compared to those of Si doped β-(Al_{0.06}Ga_{0.94})₂O₃ film grown on top of Mg-doped β-Ga₂O₃ buffer layer, clearly indicating a strong compensation of interface charges due to the introduction of Mg-doped β-Ga₂O₃ buffer layer for β -(Al_{0.06}Ga_{0.94})₂O₃ epi-film.

To investigate the influence of different carrier concentrations of β -(Al_xGa_{1-x})₂O₃ thin films on the surface morphology, AFM was performed for 6% Al composition samples grown with different doping levels as shown in Figure 5 (a-c). All the films show smooth surface morphologies with RMS roughness ranging between 0.50-1.74 nm. Although similar surface morphologies are observed, the surface roughness is found to increase from 0.50 to 1.74 nm as the doping concentration increases from 6.56×10^{17} to 1.54×10^{19} cm⁻³. The increase in surface roughness with increasing doping concentration implies crystalline quality degradation, as indicated by the

decrease in mobility values due to increased silane flow rate, revealing the strong influence of doping concentrations on the crystalline quality and electron transport properties of the films.

MOCVD growth pressure is considered as a key parameter influencing the epitaxial growth of Si doped β-(Al_xGa_{1-x})₂O₃ thin films [29]. To investigate the impact of different growth pressure on both Al and Si incorporations, several β-(Al_xGa_{1-x})₂O₃ films were grown with the chamber pressure of 20-80 torr using the same [TMAI]/[TMAI+TMGa] molar flow ratio of 1.6% and a silane flow rate of 2.66 nmole/min. The thicknesses were measured between 312-346 nm for films grown at different pressures. The XRD ω-2θ scans of β-(Al_xGa_{1-x})₂O₃ thin films in Figure 6(a) show the reduction of Al compositions from 6.3% to 3.3% as the chamber pressure increases from 20 to 80 torr. The quantitative SIMS characterization on a multi-layer stack of β-(Al_xGa_{1-x})₂O₃ grown with various chamber pressure (20 to 80 torr) reveals that the Si concentration increases with the increase of chamber pressure (Figure 6(b)), indicating higher efficiency of Si incorporation as the Al compositions reduces due to higher growth pressure. The room temperature Hall measurements on these four samples grown with chamber pressure of 20-80 torr show an increasing trend of carrier concentration and Hall mobility as the Al composition decreases with the increase of chamber pressures (Figure 6(c)), which is in a good agreement with the SIMS result (Figure 6(b)) that shows higher Si incorporation for higher pressure.

One challenge associated with the MOCVD epitaxy of β -(Al_xGa_{1-x})₂O₃ films on top of Ga₂O₃ substrate is from the formation of cracking due to the tensile strain in the β -(Al_xGa_{1-x})₂O₃ epi-films. With the increase of Al compositions, due to the increase of lattice mismatch with underneath β -Ga₂O₃ layer, the accumulated strains in β -(Al_xGa_{1-x})₂O₃ films release through the formation of cracking when the films are grown beyond their critical thicknesses [51]. To better probe the formation of the crackings, β -(Al_xGa_{1-x})₂O₃ films with Al compositions of 11% and 18% were

characterized using atomic resolution high-angle annular dark-field (HAADF) STEM imaging, as shown in Figure 7. Although uniform Al distribution with sharp β -(Al_xGa_{1-x})₂O₃/ β -Ga₂O₃ interfaces are observed for both 11% and 18% Al composition samples in atomic resolution high magnification STEM images (Figures 7(b) and (d)), the films exhibit noticeable crackings as the strain in β -(Al_xGa_{1-x})₂O₃ can no longer be accommodated elastically (Figures 7(a) and (c)). Once formed, the crackings are found to extend towards the underneath β -Ga₂O₃ layer.

To better understand the physical insights into the cracking planes, the macroscopic surface morphology of β -(Al_xGa_{1-x})₂O₃ film grown with 11% Al composition was characterized by optical microscope imaging as shown in Figure 8. Most of the crackings are directed along [001] direction which is parallel to the (100) primary cleavage plane that has the lowest surface energy [51]. The lowest surface energy of (100) cleavage plane is due to the fact that the (100) surface cuts through easily broken soft Ga(II)-O bonds in the GaO₆ octahedron. Even though most of the crackings are oriented along [001] direction, some are also found oriented along [100] direction which is parallel to the (001) cleavage plane. Due to the higher density of dangling-bonds, even though the (001) surface cuts the same Ga(II)-O bonds similar to the (100) surface, the surface energy for (001) is much higher than (100) plane, which leads to fewer cracking formation along [100] direction as compared to the [001] direction.

To investigate the effect of the crackings on electrical properties, differently oriented Hall bar structures were processed. Orientation dependent resistivity measurements were performed for β-(Al_xGa_{1-x})₂O₃ films grown with 6%, 11% and 18% Al compositions as shown in Figure 9. Hereby, mesa was etched using BCl₃/Ar (35sccm/5sccm) ICP-RIE dry etching (30 W/ 200 W) and ohmic contacts were deposited via electron beam evaporation of Ti/Au 30nm/70nm with a subsequent RTA annealing at 470°C in N₂ for 1 min. The 6% and 11% Al composition samples were grown

with 5.84 nmole/min silane flow, whereas the 18% Al composition sample was grown with 100.1 nmole/min silane flow. The minimum resistivity increases from 0.02 to 0.55 ohm-cm as the Al composition increases from 6% to 18% as shown in Figures 9(a-c). Highly homogeneous and isotropic behavior in terms of resistivity is observed for β -(Al_xGa_{1-x})₂O₃ films with 6% Al composition without crackings. However, strong anisotropic behavior has been observed for 11% and 18% Al composition samples. The smaller resistivity along [001] direction is due to the fact that (100) is the primary crack plane for (010) β -(Al_xGa_{1-x})₂O₃ films which is parallel to [001] direction (Figure 8). As most of the crackings are formed along [001] direction, the significantly higher resistivities along other directions cutting through the (100) planes provide valuable information related to the in-plane orientations of the films which can be useful to understand the orientation dependent fundamental properties of β -(Al_xGa_{1-x})₂O₃, especially in cases when the cracks are not visible from microscopic imaging.

Conclusion

In summary, the MOCVD epitaxy and fundamental characteristics of Si-doping in (010) β -(Al_xGa_{1-x})₂O₃ films were investigated in terms of structural, morphological and transport properties as a function of Al composition. Room temperature Hall mobility of 101 cm²/V.s at a net charge concentration of 6.56×10^{17} cm⁻³ was measured for uniformly doped β -(Al_xGa_{1-x})₂O₃ films with 6% Al composition. Temperature dependent Hall measurement has revealed a low temperature peak mobility of 1157 cm²/V.s at 65 K for a β -(Al_{0.06}Ga_{0.94})₂O₃ film. The SIMS depth profile indicates reduced incorporation efficiency of Si for AlGaO films with higher Al compositions. Besides, unintentional incorporation of C and H impurities, which act as compensating acceptors in β -(Al_xGa_{1-x})₂O₃, increase with the increase of Al composition, leading

to a significantly lower net carrier concentration as measured from Hall measurements for samples with higher Al composition. The influence of growth pressure on Al and Si incorporation has been studied which reveals lowering pressure can lead to higher Al composition with reduced Si incorporation. The surface roughness is found to increase with the increase of carrier concentration for the same Al composition, indicating a strong dependence of doping concentration on surface morphology. The films with higher Al compositions exhibit obvious cracking from the cross-sectional STEM and optical macroscopic surface images. Due to the lowest surface energy of (100) cleavage plane, most of the crackings are found to form along the [001] direction, leading to highly anisotropic and inhomogeneous resistivity in β -(Al_xGa_{1-x})₂O₃ films. This study will provide guidance for the precise control of n-type doping of β -(Al_xGa_{1-x})₂O₃ films with various Al compositions for future device design and fabrication based on β -(Al_xGa_{1-x})₂O₃/ β -Ga₂O₃ heterostructures.

Conflict of Interest Statement

On behalf of all authors, the corresponding author states that there is no conflict of interest.

Acknowledgements

The authors acknowledge the Air Force Office of Scientific Research FA9550-18-1-0479 (AFOSR, Dr. Ali Sayir) for financial support. The authors also acknowledge the National Science Foundation (Grant No. 1810041, No. 2019753) and Semiconductor Research Corporation (SRC) under the Task ID GRC 3007.001 for partial support.

Data Availability

The data that support the findings of this study are available from the corresponding author upon reasonable request.

References

- 1. M. Higashiwaki and G. H. Jessen, Appl. Phys. Lett. 112, 060401 (2018).
- 2. A. Kuramata, K. Koshi, S. Watanabe, Y. Yamaoka, T. Masui, and S. Yamakoshi, Jpn. J. Appl. Phys., Part 1 55, 1202A2 (2016).
- 3. Z. Feng, A F M A. U. Bhuiyan, M. R. Karim, and H. Zhao, Appl. Phys. Lett. 114, 250601 (2019).
- 4. H. Okumura, M. Kita, K. Sasaki, A. Kuramata, M. Higashiwaki, and J. S. Speck, Appl. Phys. Express 7, 095501 (2014).
- 5. E. Ahmadi, O. S. Koksaldi, S. W. Kaun, Y. Oshima, D. B. Short, U. K. Mishra and J. S. Speck, Appl. Phys. Express 10, 041102 (2017).
- 6. Z. Feng, A F M A. U. Bhuiyan, Z. Xia, W. Moore, Z. Chen, J. F. McGlone, D. R. Daughton, A. R. Arehart, S. A. Ringel, S. Rajan, and H. Zhao, Phys. Status Solidi RPL. 14, 2000145 (2020).
- 7. H. Ghadi, J. F. McGlone, Z. Feng, A. F. M. A. U. Bhuiyan, H. Zhao, A. R. Arehart, S. A. Ringel, Appl. Phys. Lett. 117, 172106 (2020).
- 8. A. Bhattacharyya, P. Ranga, S. Roy, J. Ogle, L. Whittaker-Brooks, and S. Krishnamoorthy, Applied Physics Letters 117, 142102 (2020).
- 9. G. Seryogin, F. Alema, N. Valente, H. Fu, E. Steinbrunner, A. T. Neal, S. Mou, A. Fine, and A. Osinsky, Appl. Phys. Lett. 117, 262101 (2020).
- 10. H. Ghadi, J. F. McGlone, C. M Jackson, E. Farzana, Z. Feng, A. F. M. A. U. Bhuiyan, H. Zhao, A. R Arehart, S. A. Ringel, APL Materials 8, 021111 (2020).
- 11. Z. Xia, H. Xue, C. Joishi, J. McGlone, N. K. Kalarickal, S. H. Sohel, M. Brenner, A. Arehart, S. Ringel, S. Lodha, W. Lu, and S. Rajan, IEEE Electron Device Lett. 40, 1052 (2019).
- 12. E. Farzana, F. Alema, W. Y. Ho, A. Mauze, T. Itoh, A. Osinsky, J. S Speck, Appl. Phys. Lett. 118, 162109 (2021).
- 13. Z. Hu, K. Nomoto, W. Li, N. Tanen, K. Sasaki, A. Kuramata, T. Nakamura, D. Jena, and H. G. Xing, IEEE Electron Device Lett. 39, 869 (2018).
- 14. M. Higashiwaki, K. Sasaki, A. Kuramata, T. Masui, and S. Yamakoshi, Appl. Phys. Lett. 100, 013504 (2012).
- 15. J. Green, K. D. Chabak, E. R. Heller, R. C. Fitch, Jr., M. Baldini, A. Fiedler, K. Irmscher, G. Wagner, Z. Galazka, S. E. Tetlak, A. Crespo, K. Leedy, and G. H. Jessen, IEEE Electron Device Lett. 37, 902 (2016).
- 16. T. Oshima, T. Okuno, N. Arai, N. Suzuki, S. Ohira, and S. Fujita, Appl. Phys. Express 1, 011202 (2008).

- 17. Z. Feng, A F M A. U. Bhuiyan, N. K. Kalarickal, S. Rajan, and H. Zhao, Phys. Appl. Phys. Lett. 117, 222106 (2020).
- 18. N. K Kalarickal, A. Fiedler, S. Dhara, H.-L. Huang, A F M A. U. Bhuiyan, M. W. Rahman, T. Kim, Z. Xia, Z. J. Eddine, A. Dheenan, M. Brenner, H. Zhao, J. Hwang, S. Rajan, Appl. Phys. Lett. 119, 123503 (2021).
- 19. Y. Zheng, Z. Feng, A F M A. U. Bhuiyan, L. Meng, S. Dhole, Q. Jia, H. Zhao, J.-H. Seo, J. Mater. Chem. C. 9, 6180 (2021).
- 20. H. Peelaers, J. B. Varley, J. S. Speck, and C. G. Van de Walle, Appl. Phys. Lett. 112, 242101 (2018).
- 21. S. W. Kaun, F. Wu, and J. S. Speck, J. Vac. Sci. Technol. A 33, 041508 (2015).
- 22. T. Oshima, T. Okuno, N. Arai, Y. Kobayashi, and S. Fujita, Jpn. J. Appl. Phys. Part 1 48, 070202 (2009).
- 23. P. Vogt, A. Mauze, F. Wu, B. Bonef, and J. S. Speck, Appl. Phys. Express 11, 115503 (2018).
- 24. A F M A. U. Bhuiyan, Z. Feng, J. M. Johnson, Z. Chen, H.-L. Huang, J. Hwang, and H. Zhao, Appl. Phys. Lett. 115, 120602 (2019).
- 25. A F M A. U. Bhuiyan, Z. Feng, J. M. Johnson, H.-L. Huang, J. Sarker, M. Zhu, M. R. Karim, B. Mazumder, J. Hwang, and H. Zhao, APL Mater. 8, 031104 (2020).
- 26. A F M A. U. Bhuiyan, Z. Feng, J. M. Johnson, H.-L. Huang, J. Hwang, and H. Zhao, Cryst. Growth Des. 20, 6722 (2020).
- 27. A F M A. U. Bhuiyan, Z. Feng, J. M. Johnson, H.-L. Huang, J. Hwang, and H. Zhao, Appl. Phys. Lett. 117, 252105 (2020).
- 28. A F M A. U. Bhuiyan, Z. Feng, J. M. Johnson, H.-L. Huang, J. Hwang, and H. Zhao, Appl. Phys. Lett. 117, 142107 (2020).
- 29. A F M A. U. Bhuiyan, Z. Feng, L. Meng, H. Zhao, J. Mater. Res. 36, 4804 (2021).
- 30. J. M. Johnson, H.-L. Huang, M. Wang, S. Mu, J. B. Varley, A. F. M. A. U. Bhuiyan, Z. Feng, N. K. Kalarickal, S. Rajan, H. Zhao, C. G. Van de Walle, and J. Hwang, APL Materials 9, 051103 (2021).
- 31. A F M A. U. Bhuiyan, Z. Feng, J. M. Johnson, H.-L. Huang, J. Sarker, M. Zhu, M. R. Karim, B. Mazumder, J. Hwang, and H. Zhao, APL Materials 8 (8), 089102 (2020).
- 32. J. Sarker, A. F. M. A. U. Bhuiyan, Z. Feng, H. Zhao and B. Mazumder, J. Phys. D: Appl. Phys. 54, 184001 (2021).
- 33. A F M A. U. Bhuiyan, Z. Feng, H.-L. Huang, L. Meng, J. Hwang, H. Zhao, J. Vac. Sci. Technol. A 39, 063207 (2021).
- 34. J. Sarker, S. Broderick, A. F. M. A. U. Bhuiyan, Z. Feng, H. Zhao, and B. Mazumder, Appl. Phys. Lett. 116, 152101 (2020).
- 35. S. Krishnamoorthy, Z. Xia, C. Joishi, Y. Zhang, J. McGlone, J. Johnson, M. Brenner, A. R. Arehart, J. Hwang, S. Lodha, and S. Rajan, Appl. Phys. Lett. 111, 023502 (2017).

- 36. Y. Zhang, A. Neal, Z. Xia, C. Joishi, J. M. Johnson, Y. Zheng, S. Bajaj, M. Brenner, D. Dorsey, K. Chabak, G. Jessen, J. Hwang, S. Mou, J. P. Heremans, and S. Rajan, Appl. Phys. Lett. 112, 173502 (2018).
- 37. N. K. Kalarickal, Z. Feng, A F M A. U. Bhuiyan, Z. Xia, J. F. McGlone, W. Moore, A. R. Arehart, S. A. Ringel, H. Zhao, and S. Rajan, IEEE Transaction on Electron Devices, 68, 29-35 (2021).
- 38. P. Ranga, A. Bhattacharyya, A. Rishinaramangalam, Y. K Ooi, M. A. Scarpulla, D. Feezell and S. Krishnamoorthy, Appl. Phys. Express 13, 045501 (2020).
- 39. P. Ranga, A. Bhattacharyya, A. Chmielewski, S. Roy, R. Sun, M. A Scarpulla, N. Alem, and S. Krishnamoorthy, Appl. Phys. Express 14, 025501 (2021).
- 40. J. B. Varley, J. Mater. Res. 36, 4790 (2021).
- 41. J. B. Varley, A. Perron, V. Lordi, D. Wickramaratne, and J. L. Lyons, Appl. Phys. Lett. 116, 172104 (2020).
- 42. S. Mu, M. Wang, J. B. Varley, J. L. Lyons, D. Wickramaratne, and C. G. Van de Walle, arXiv:2111.07194v1 (2021).
- 43. P. Ranga, A. Rishinaramangalam, J. Varley, A. Bhattacharyya, D. Feezell, and S. Krishnamoorthy, Appl. Phys. Express 12, 111004 (2019).
- 44. J. L. Lyons, D. Steiauf, A. Janotti, and C. G. Van de Walle, Phys. Rev. Applied 2, 064005 (2014).
- 45. A. Hernandez, M. M. Islam, P. Saddatkia, C. Codding, P. Dulal, S. Agarwal, A. Janover, S. Novak, M. Huang, T. Dang, M. Snure, F.A. Selim, Results Phys. 25, 104167 (2021).
- 46. K. Ikenaga, N. Tanaka, T. Nishimura, H. Iino, K. Goto, M. Ishikawa, H. Machida, T. Ueno, and Y. Kumagai, J. Cryst. Growth 582, 126520 (2022).
- 47. J. M. Johnson, Z. Chen, J. B. Varley, C. M. Jackson, E. Farzana, Z. Zhang, A. R. Arehart, H-LHuang, A Genc, S. A. Ringel, C. G. Van de Walle, D. A. Muller, and J. Hwang, Phys. Rev. X 9, 041027 (2019).
- 48. A. T. Neal, S. Mou, S. Rafique, H. Zhao, E. Ahmadi, J. S. Speck, K. T. Stevens, J. D. Blevins, D. B. Thomson, N. Moser, K. D. Chabak, and G. H. Jessen, Appl. Phys. Lett. 113, 062101 (2018).
- 49. S. Bharadwaj, S. M. Islam, K. Nomoto, V. Protasenko, A. Chaney, H. G. Xing, and D. Jena, Appl. Phys. Lett. 114, 113501 (2019).
- 50. J. L. Lyons, Semicond. Sci. Technol. 33, 05LT02 (2018).
- 51. S. Mu, M. Wang, H. Peelaers, and C. G. Van de Walle, APL Mater. 8, 091105 (2020).

Table Captions

Table 1. SIMS impurity concentrations of Si, C, H, and Cl in β -(Al_xGa_{1-x})₂O₃ films grown with 6% and 18% Al compositions.

Table 2. The room temperature carrier concentration and Hall mobility of Si doped β-(Al_xGa_{1-x})₂O₃ films with 6% and 18% Al compositions grown on Mg doped β-Ga₂O₃ buffer layer with silane flow rates of 5.84 and 14.35 nmole/min.

Figure Captions

Figure 1. (a) Schematic structure of β -(Al_xGa_{1-x})₂O₃ thin film grown on Mg doped β -Ga₂O₃ buffer layer on top of (010) β -Ga₂O₃ substrate. (b) XRD ω-2θ scans of (010) β -(Al_xGa_{1-x})₂O₃ films grown with Al compositions of 6%, 11% and 18%.

Figure 2. (a) Schematic of the sample layer stack consisting of Si doped β-(Al_xGa_{1-x})₂O₃ and UID β-Ga₂O₃. (b) The SIMS impurity depth profiles for Si doped β-(Al_xGa_{1-x})₂O₃ layers grown with 6% and 18% Al compositions.

Figure 3. (a) Room temperature Hall mobility and resistivity as a function of carrier concentration measured from β -(Al_xGa_{1-x})₂O₃ thin films grown with 6% Al composition. Temperature dependent (b) carrier mobility as a function of temperature and (c) carrier concentration as a function of reciprocal temperature for Si doped β-(Al_xGa_{1-x})₂O₃ films with 6% Al composition. The symbols are the measured data, and the solid black line in (c) represents the fitting of the carrier density profile calculated from the charge neutrality equation.

Figure 4: Comparison of the temperature dependent carrier concentration profiles as a function of reciprocal temperature for Si doped β -(Al_{0.06}Ga_{0.94})₂O₃ film grown on Mg-doped β -Ga₂O₃ buffer layer and β -(Al_{0.18}Ga_{0.82})₂O₃ film grown on UID β -Ga₂O₃ buffer layer, indicating a strong compensation of interface charges due to the introduction of Mg-doped β -Ga₂O₃ buffer layer.

Figure 5. The surface AFM images of 6% Al content Si doped β-(Al_xGa_{1-x})₂O₃ films with carrier concentrations of (a) $6.56x10^{17}$ cm⁻³, (b) $5.30x10^{18}$ cm⁻³ and (c) $1.54x10^{19}$ cm⁻³.

Figure 6. (b) XRD ω-2θ scans of (010) β-(Al_xGa_{1-x})₂O₃ films grown at different growth pressures of 20-80 torr, indicating the reduction of Al compositions from 6.3% to 3.3% with increasing pressure. (b) Si impurity concentration of β-(Al_xGa_{1-x})₂O₃ films extracted from SIMS on the

sample layer stack of β -(Al_xGa_{1-x})₂O₃ grown with different chamber pressure (20-80 torr) (c) The room temperature carrier concentration and hall mobility as a function of growth pressure. The SIMS sample stack and all β -(Al_xGa_{1-x})₂O₃ films in (a) and (c) are grown with [TMA1]/[TMA1+TMGa] molar flow ratio of 1.6% and a silane flow rate of 2.66 nmole/min.

Figure 7. Atomic resolution HAADF-STEM cross-sectional images of β -(Al_xGa_{1-x})₂O₃ films grown with Al compositions of (a,b) 11% and (c,d) 18%. The HAADF-STEM images were taken from [001] zone axis.

Figure 8. Optical macroscopic surface morphology of β -(Al_xGa_{1-x})₂O₃ film grown with 11% Al composition showing cracks along [001] direction parallel to the (100) primary cleavage plane.

Figure 9. The directional dependence of the resistivity measured for β-(Al_xGa_{1-x})₂O₃ film grown with Al compositions of (a) 6%, (b) 11% and (c) 18%, indicating strong anisotropic behavior of high Al content β-(Al_xGa_{1-x})₂O₃ films in terms of resistivity along different directions.

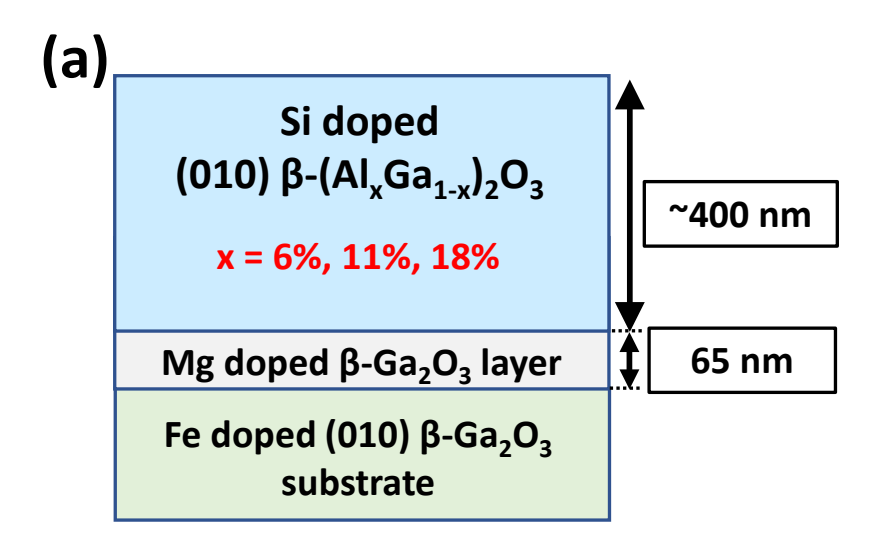
Table 1.

Element	Average concer	Average concentrations (cm ⁻³)	
	A1 = 6%	A1 = 18%	
Si	8×10 ¹⁷	5×10 ¹⁷	1×10 ¹⁵
C	4×10^{16}	1.5×10^{17}	2×10^{16}
Н	8×10^{15}	1×10^{17}	5×10^{15}
C1	1.5×10^{14}	6×10^{14}	2×10^{14}

Table 2.

Sample	Silane flow rates	Al composition	Carrier Concentration	Mobility
	(nmole/min)	(%)	(cm^{-3})	$(cm^2/V \cdot s)$
1	5.84	6	4.90×10^{18}	57
2	5.84	18	2.46×10^{15}	15
3	14.35	6	1.54×10^{19}	54
4	14.35	18	2.11×10^{17}	3

Figure 1.



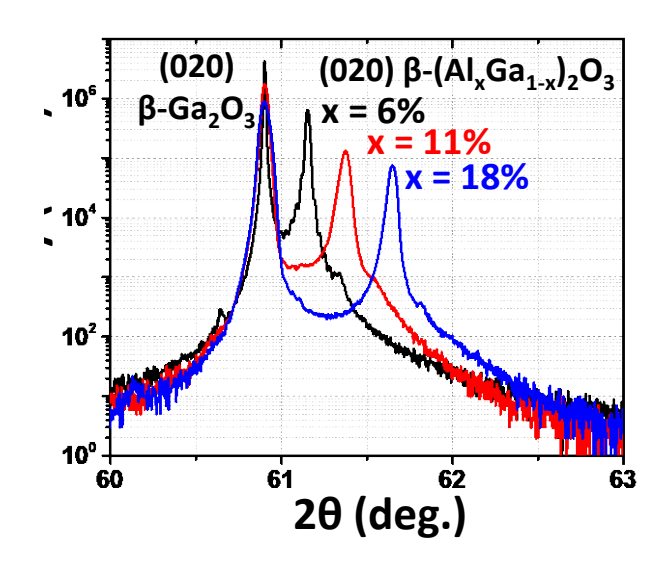
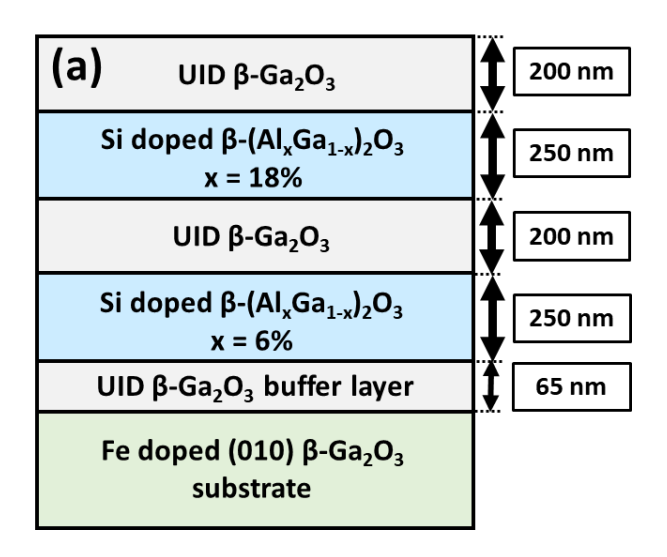


Figure 2.



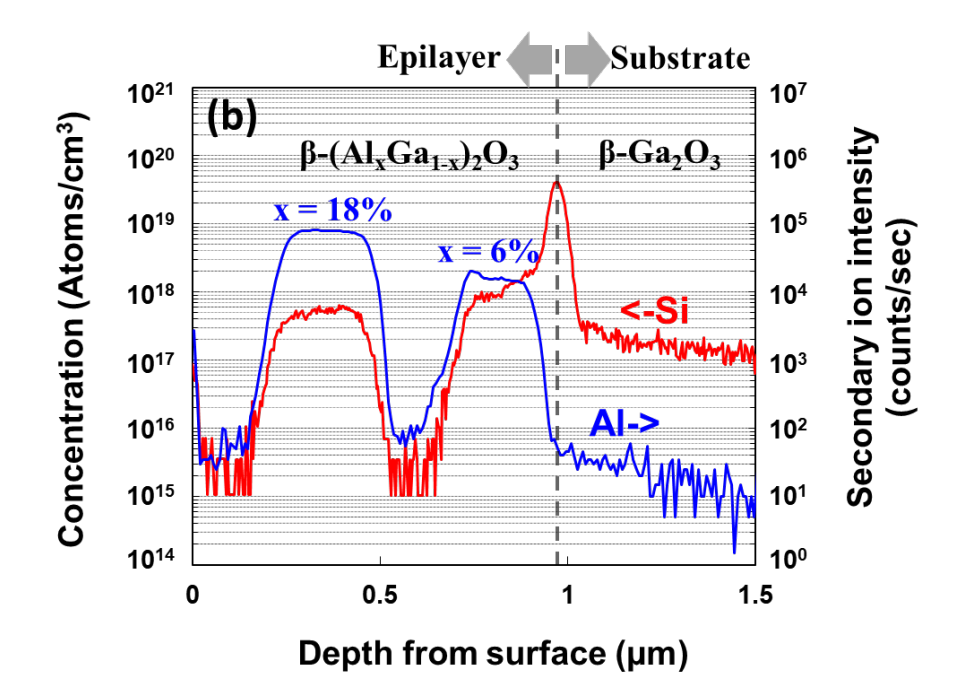
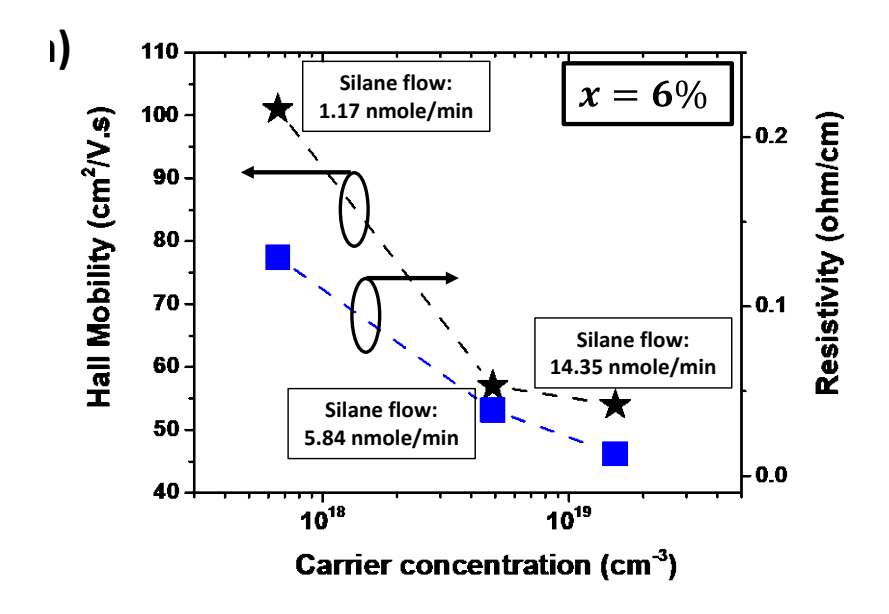


Figure 3.



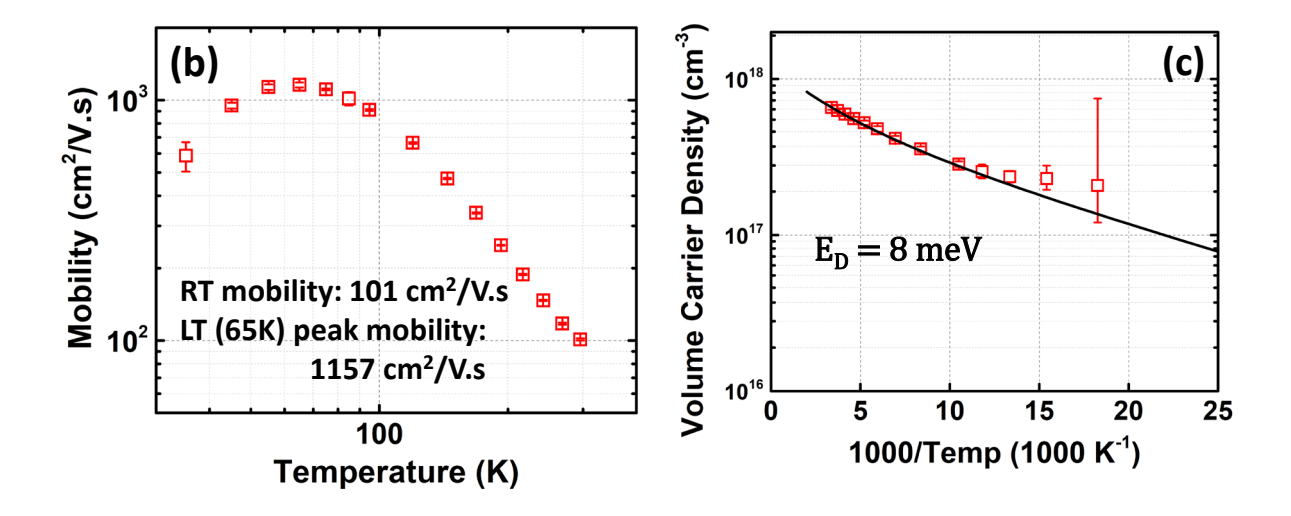


Figure 4.

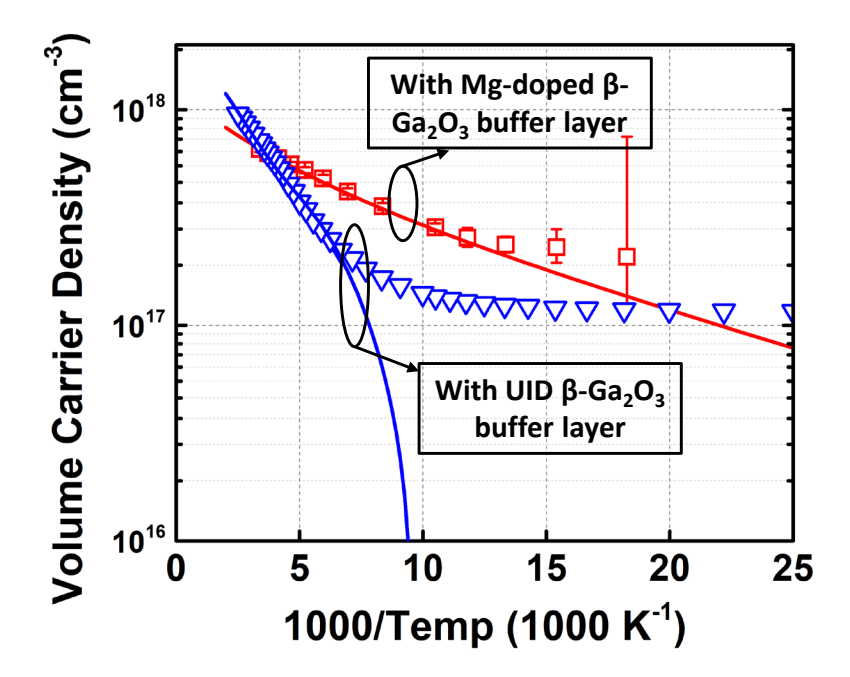


Figure 5.

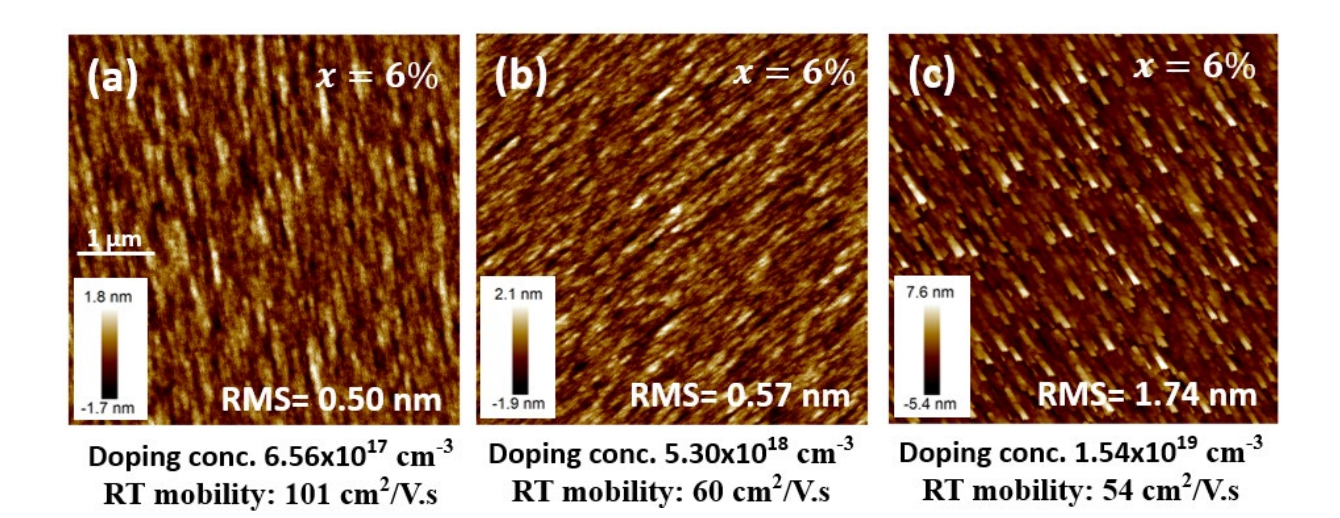


Figure 6.

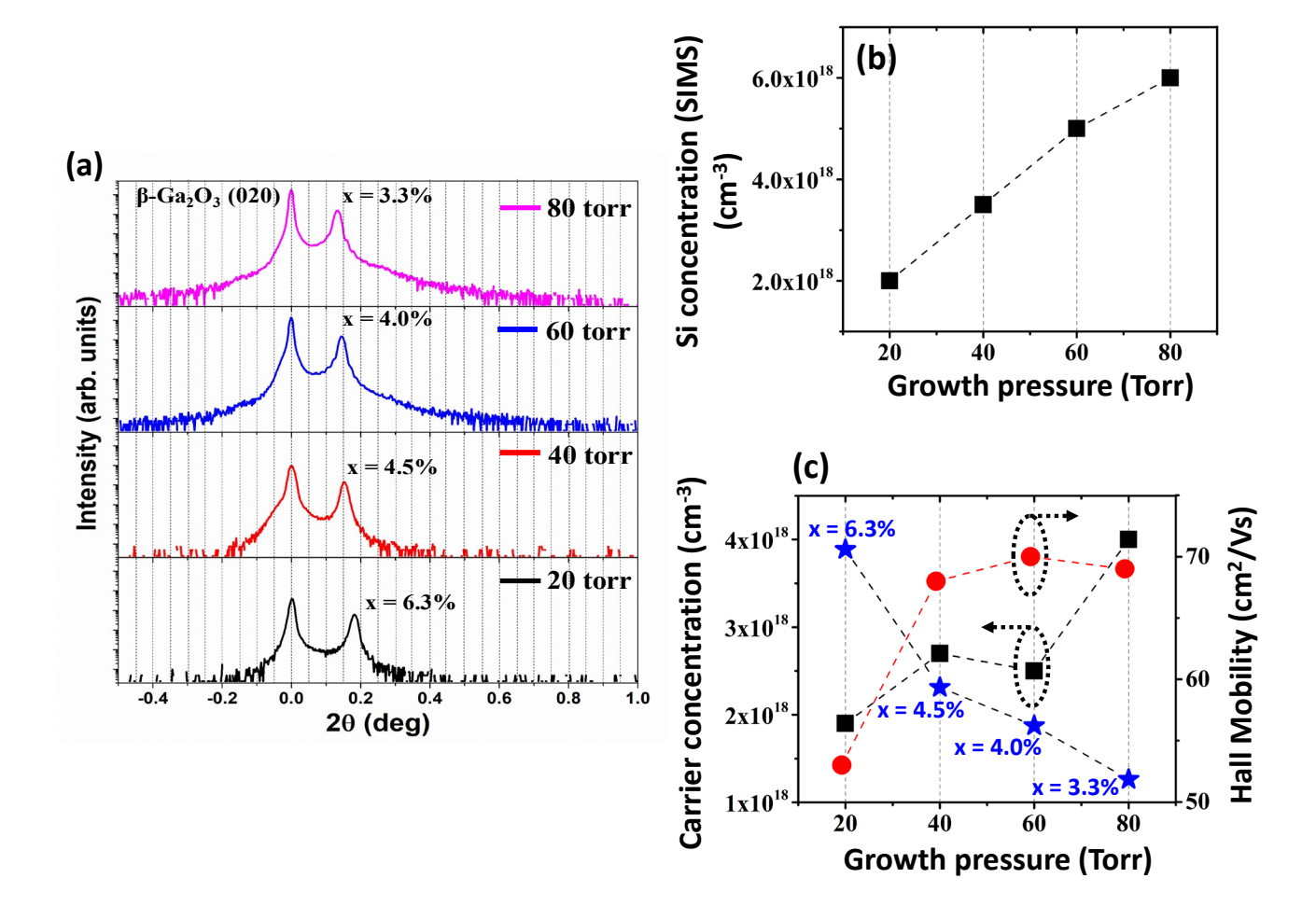


Figure 7.

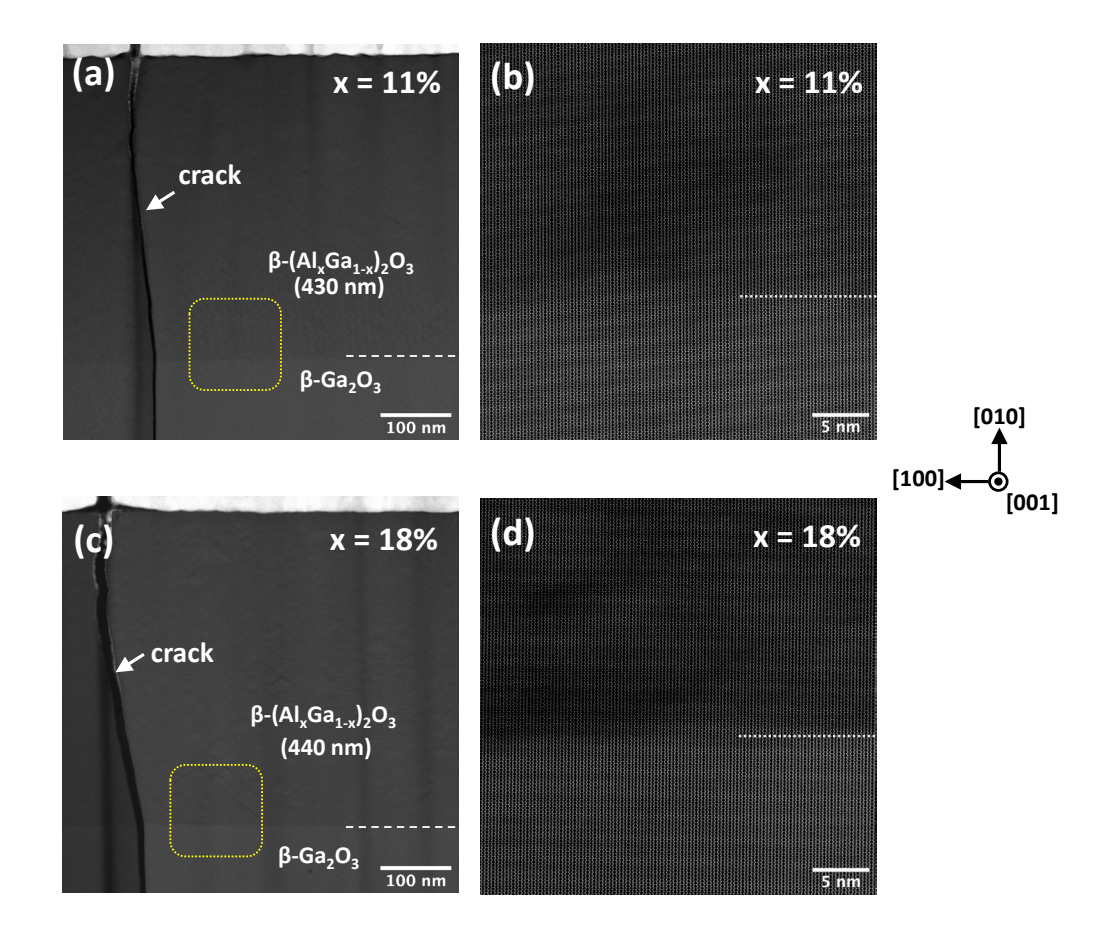


Figure 8.

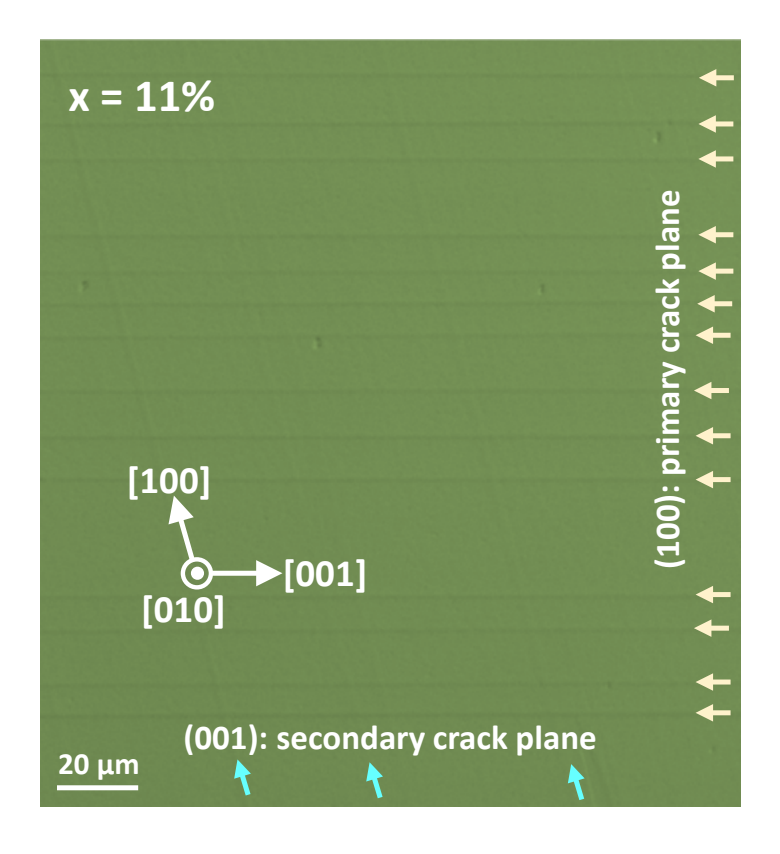


Figure 9.

